Abed, Ayman; Sołowski, Wojciech Tomasz

Applications of the new thermo-hydro-mechanical-chemical coupled code 'Thebes'

Published in:
Environmental Geotechnics

DOI:
10.1680/jenge.18.00083
10.1680/jenge.18.00083

Published: 18/02/2020

Document Version
Peer-reviewed accepted author manuscript, also known as Final accepted manuscript or Post-print

Please cite the original version:
Abed, A., & Sołowski, W. T. (2020). Applications of the new thermo-hydro-mechanical-chemical coupled code 'Thebes'. *Environmental Geotechnics* , *7*(1), 3-16. Article 1800083. https://doi.org/10.1680/jenge.18.00083, https://doi.org/10.1680/jenge.18.00083

Applications of a New THMC Coupled Code “Thebes”

Author 1

- Ayman A. Abed Dr.-Ing, MSc, BSc
- Postdoctoral Researcher, Department of Civil Engineering, Aalto University, Espoo, Finland
- ORCID number

Author 2

- Wojciech T. Sołowski PhD, MSc
- Assistant Professor, Department of Civil Engineering, Aalto University, Espoo, Finland
- ORCID number

Full contact details of corresponding author.

Aalto University, Department of Civil Engineering, P.O.Box 12100, FI-00076 Aalto, Finland

E-mail: ayman.abed@aalto.fi

Abstract

This contribution presents two numerical applications of a newly developed fully coupled thermo-hydro-mechanical-chemical (THMC) finite element code (Thebes Code). The paper starts with an introduction of the adopted theoretical framework and its implementation followed by the description of the performed simulations. The first application involves the modelling of a large-scale mock-up test performed by CIEMAT (Madrid, Spain) which also serves as a validation benchmark. In the second application, the paper shows the solution of the Elder problem, which verifies the code capability to capture the density-driven salt transport triggered by the hydro-chemical coupling. The results of both simulations are in good agreement with the published data and the experimental measurements, serving as a further validation of the theoretical assumptions and verification of the correctness of the code implementation.

Keywords chosen from ICE Publishing list
Environmental engineering; finite-element modelling; radioactive waste disposal

List of notation

Roman

a	Fitting parameter
$\boldsymbol{b}$	Body force vector, [M L T^{-2}]
C	Concentration in liquid phase, [M L^{-3}]
C_{max}	Maximum concentration, [M L^{-3}]
C_s	Concentration in solid phase, [M M^{-1}]
$\boldsymbol{D}^e$	Elastic stiffness matrix
D_{atm}	Molecular diffusivity of water vapour in air, [L^2 T^{-1}]
D_o	Molecular diffusion coefficient, [L^2 T^{-1}]
D_h	Dispersion coefficient, [L^2 T^{-1}]
D_{vT}	Molecular diffusivity due to temperature, [M L^{-1} T^{-1} Θ^{-1}]
D_{vw}	Molecular diffusivity due to moisture, [M L^{-2} T^{-1}]
F	Yield function
f_{Tv}	Thermal enhancement factor
e	Euler's number or Napier's constant
g	earth gravity acceleration, [L T^{-2}]
g_α, g_n, g_m	van Genuchten curve fitting parameters
H	Henry's volumetric coefficient of solubility
h_g	Gas pressure head, [L]
h_w	Water pressure head, [L]
$\boldsymbol{j}_k^i$	Non-advective flux of component k, [M L^{-2} T^{-1}]
k	BBM parameter
K_d	Distribution coefficient, [L^3 M^{-1}]
K^l	Liquid phase hydraulic conductivity, [L T^{-1}]
K_{sat}^l	Liquid phase saturated hydraulic conductivity, [L T^{-1}]
L	Latent heat of water vaporization, [L^2 T^{-2}]
M	Slope of critical state line
$\boldsymbol{m}$	Auxiliary vector, {1,1,1,0,0,0}
n	Porosity
P_{atm}	Atmospheric pressure, [M L^{-1} T^{-2}]
p_o	Isotropic preconsolidation pressure, [M L^{-1} T^{-2}]
p	Mean net pressure, [M L^{-1} T^{-2}]
p_{ref}^o	Reference mean pressure, [M L^{-1} T^{-2}]
p_o^*	Saturated isotropic preconsolidation pressure at reference temperature, [M L^{-1} T^{-2}]
p_{oi}^*	Saturated isotropic Preconsolidation pressure at the beginning of loading step i, [M L^{-1} T^{-2}]
p_{oT}^*	Saturated isotropic preconsolidation pressure at temperature T, [M L^{-1} T^{-2}]
p^c	Reference pressure in BBM, [M L^{-1} T^{-2}]
p_w	Water pressure, [M L^{-1} T^{-2}]
p_{wo}	Reference water pressure, [M L^{-1} T^{-2}]
Q	Plastic potential function
Q_k^i	Sink/source term of component k, [M L^{-3} T^{-1}]
$\boldsymbol{q}$	Darcy velocity, [L T^{-1}]
q	Deviatoric stress, [M L^{-1} T^{-2}]
$\boldsymbol{q}_h$	Total heat flux, [M T^{-3}]
$\boldsymbol{q}^T$	Conductive heat flux, [M T^{-3}]
r	BBM parameter
S^i	Degree of saturation ($i = l, g$)
s	Suction, [M L^{-1} T^{-2}]
T	Absolute temperature, [Θ]
$\mathrm{tr}(\,)$	Trace operator
v	Specific volume
$\boldsymbol{v}^i$	Velocity of phase i, [L T^{-1}]
T_o	Reference absolute temperature, [Θ]
t	Time, [T]

Greek

α	Dispersivity, [L^{-1}]
α^*	BBM non-associate plasticity coefficient
α_o, α_2	Elastic thermal strain parameters in BBM
α_1, α_3	Parameters control thermal effects on preconsolidation pressure in BBM
α_κ	Parameter controls κ value in BBM
$\alpha_{\kappa s1}, \alpha_{\kappa s2}$	Parameters control κ_s value in BBM
β_{sT}	Coefficient of volumetric thermal expansion of solid particles, Θ^{-1}
β_{wp}	Coefficient of water compressibility, [M^{-1} L T^2]
β_{wT}	Coefficient of volumetric thermal expansion of water, [Θ^{-1}]
β	BBM parameter, [M^{-1} L T^2]
β^*	Factor of water salinity
Δ	Increment
$\boldsymbol{\varepsilon}$	Strain vector
ε_v	Infinitesimal volumetric strain
κ	Isotropic swelling index
κ_o	Reference isotropic swelling index
κ_s	Swelling index due to suction
κ_{so}	Reference swelling index due to suction
Λ	Plastic multiplier
λ	Isotropic compression index at full saturation
λ_{dry}	Thermal conductivity of a completely dry material, [M L T^{-3} Θ^{-1}]
λ_s	Isotropic compression index at a constant suction
λ_{sat}	Thermal conductivity of a fully saturated material, [M L T^{-3} Θ^{-1}]
λ_T	Thermal conductivity, [M L T^{-3} Θ^{-1}]
ν	Poisson's ratio
μ_l	Liquid phase dynamic viscosity, [M L^{-1} T^{-1}]
ρ_a	Dry air density, [M L^{-3}]
ρ^i	Density of phase i, [M L^{-3}]
ρ_k^i	Density of component k in phase i, [M L^{-3}]
ρ_{wo}^l	Reference water density, [M L^{-3}]
ρ_{wf}^l	Density of distilled water, [M L^{-3}]
ρ^s	Solid particles density, [M L^{-3}]
ρ^T	Thermal BBM parameter
$\boldsymbol{\sigma}$	Net stress vector, [M L^{-1} T^{-2}]
σ^t	Surface tension of water, [M T^{-2}]
σ_o^t	Reference surface tension, [M T^{-2}]
$\boldsymbol{\sigma^{tot}}$	Total stress tensor, [M L^{-1} T^{-2}]
τ	Tortuosity
ω_k^i	Mass fraction of component k in phase i
ξ_n^T	Curve fitting parameter, [Θ^{-1}]
ξ_w^T	Curve fitting parameter, [Θ^{-1}]
ψ	Matric suction head, [L]
γ_T	Material constant
Φ_h	Soil heat capacity, [M L^{-1} T^{-2}]
ϕ^i	Volume fraction of phase i
$\langle\cdot\rangle$	Derivation with respect to time
∂	Partial differentiation operator
$\boldsymbol{\nabla}$	Gradient operator
$\boldsymbol{\nabla}\cdot$	Divergence operator

Superscripts

e	elastic
g	Gas phase
i	Phase (i = s - solid, l - liquid, g - gas)
l	Liquid phase
s	Solid phase
tot	Total
v	Volumetric

Subscripts

a	Dry air component
g	Gas phase
k	Component ($k = a, w, s, st$)
sp	Solid particles component
st	Salt component
T	Temperature
w	Water component

Note: The units are given after the comma, where L, M, T and Θ mean units of length, mass, time and temperature, respectively.

1. Introduction

Safe design of engineering barriers requires knowledge and consideration of the influencing processes during the expected life cycle of the facility. In the case of a final disposal site for the spent nuclear fuel, the bentonite used as a sealing barrier must provide sustainable protection to the surrounding environment from the hazardous waste effect for hundreds of thousands of years. It is widely recognized that an acceptable simulation of the bentonite (or any other geomaterial) response in such complex environmental conditions should sufficiently address the effects of the active processes represented by the thermo-hydro-mechanical-chemical (THMC) coupled behaviour. This topic has been the focus of many research groups (e.g. Olivella *et al.*, 1996; Rutqvist *et al.*, 2001; Collin *et al.*, 2002; Laloui *et al.*, 2003; Seetharam *et al.*, 2007; Sánchez *et al.*, 2017; Jacinto and Ledesma, 2017; Abed and Sołowski, 2017; Ahmad, 2017; Toprak *et al.*, 2018; Rodriguez-Dono *et al.*, 2018; Villar *et al.*, 2018).

In this context, the authors created a new finite element code, referred to in this paper as Thebes Code, with the goal to simulate the fully coupled THMC behaviour of bentonite. The developed framework encompasses novel features that include among others: 1) a more accurate derivation of the dry air and the thermal energy balance equations; 2) a new implementation of the temperature influence on the soil water characteristic curve and 3) effects of microstructure evolution on the water retention features and hydraulic conductivity of the simulated geomaterial. For the full discussion on these new developments, implementation, verification and validation of the code, the reader is referred to Abed *et al.*(2016) and Abed and Sołowski (2017, 2018). Recently, the capabilities of Thebes Code has been extended to include simple chemical effects (Abed *et al.*, 2018) based on the theoretical work of Warrick *et al.* (1971), Van Genuchten (1982) and Boufadel *et al.* (1997).

In this contribution, the chemical part is enhanced by introducing the effect of the salt concentration on the water density, which affects the possible water flow patterns.

After presenting the governing balance equations with the adopted constitutive relationships, the paper demonstrates the capabilities of the code and the modelling framework by solving two benchmarks. The first simulation aim is to replicate the measurements of the CIEMAT mock-up test (Martin *et al.*, 2006). This test has been selected due to the well-defined boundary conditions, measured data and the good characterization of the bentonite used in the

experiment. This test was also modelled by other research groups (CODE-BRIGHT, 2002; Sánchez and Gens, 2014) providing reliable references for discussing the employed material parameters and the numerical results.

The aim of the second simulation is to verify the capability of the code to model the density-driven salt transport. This verification is done by simulating the Elder problem (Elder, 1967), a well-known benchmark that is routinely exploited for verification purposes (Voss and Souza, 1987; Boufadel *et al.*, 1999; Diersch and Kolditz, 2002; Johannsen, 2003; Simpson and Clement, 2003; Van Reeuwijk *et al.*, 2009). The provided results represent up-to-date calculations with clearly defined boundary conditions, spatial and time discretisation schemes, which might be used in the future comparisons and benchmarks.

Both benchmarks yielded very satisfactory agreement with the targeted data, which further verifies the implementation and validates the applicability of the adopted theoretical framework.

2. Governing Equations and Solution Strategy

In this section, a summary of the adopted balance equations is given. The detailed description and derivation of these equations can be found in Abed and Sołowski (2017). Sections below only discuss the mass balance of the salt component and its effect on the water density in greater detail, as these constitute the new contribution of the paper.

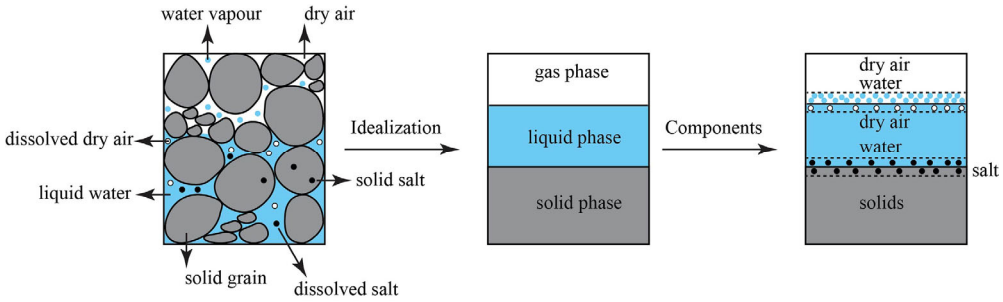

Figure 1. Phases and components of a geomaterial.

2.1 Mass balance equations

The soil is modelled as a porous medium consisting of the solid phase (s), the gas phase (g) and the liquid phase (l). Each phase has its components: (i) the solid phase has the solid soil particles (sp) and possibly crystallised (adsorbed) salt (st), (ii) the gas phase is decomposed into the dry air (a) and the water vapour (w) and (iii) the liquid phase consists of the liquid water

(w), the dissolved dry air (a) and the dissolved salt (st), see Figure 1. The compositional method (Panday and Corapcioglu, 1989) is used to derive the mass balance equations for the soil components. Accordingly, the general mass balance equation for any one component is written as (Olivella *et al.*, 1994; Diersch and Kolditz, 2002; van Esch, 2010; Huyakorn, 2012; Abed and Sołowski, 2017):

$$\underbrace{\frac{\partial\left(\phi^i\rho^i\omega_k^i\right)}{\partial t}}_{storage\ term}+\underbrace{\boldsymbol{\nabla}\cdot\left(\phi^i\rho^i\omega_k^i\boldsymbol{v}^i\right)}_{advection\ term}+\underbrace{\boldsymbol{\nabla}\cdot\boldsymbol{j}_k^i}_{non-advection\ term}=\underbrace{Q_k^i}_{sink/source\ term}$$

1.

where the symbols ϕ^i and ρ^i denote volume fraction and density of the phase i (i=solid, liquid, gas). The mass fraction of component k in the i-phase is $\omega_k^i = {\rho_k^i}/{\rho^i}$. The phase-velocity vector is represented by $\boldsymbol{v}^i$ whereas $\boldsymbol{j}_k^i$ is the non-advective flux vector of the component k. The sink or source term Q_k^i of the component k obeys the constraint $Q_k^s + Q_k^l + Q_k^g = 0$ in absence of any external sink/source. Based on Equation 1 the following balance equations for each component can be derived (see Abed and Sołowski (2017) for full details):

1. Mass balance equation of the water component:

$$-(1-n)\left(S^l\rho_w^l+S^g\rho_w^g\right)\beta_{sT}\frac{\partial T}{\partial t}+\left(S^l\rho_w^l+S^g\rho_w^g\right)\frac{\partial\varepsilon_v}{\partial t}+n\left(\rho_w^l-\rho_w^g\right)\frac{\partial S^l}{\partial t}+nS^l\frac{\partial\rho_w^l}{\partial t}+nS^g\frac{\partial\rho_w^g}{\partial t}+\boldsymbol{\nabla}\cdot\left(\rho_w^l\boldsymbol{q}^l\right)+\boldsymbol{\nabla}\cdot\left(\rho_w^g\boldsymbol{q}^g\right)+\boldsymbol{\nabla}\cdot\boldsymbol{j}_w^g=0$$

2.

where S^l and S^g denote the liquid and the gas degree of saturation, respectively. The symbols T, n, ε_v, β_{sT} stand for temperature, porosity, volumetric strain and the coefficient of solid thermal expansion, respectively. The flow velocity of the liquid phase $\boldsymbol{q}^l$ and the gas phase $\boldsymbol{q}^g$ are assumed to obey Darcy's law (Darcy, 1856).

It is important to notice that the water density ρ_w^l in this extended formulation is assumed to be a function of temperature T, water pressure p_w and salt concentration C (Boufadel *et al.*, 1999):

$$\rho_w^l = \beta^* \, \rho_{wo}^l e^{\beta_{wp}(p_w - p_{wo}) - \beta_{wT}(T - T_o)} = \beta^* \, \rho_{wf}^l$$

3.

with

$$\beta^* = \left(1 + a\frac{C}{C_{max}}\right)$$

4.

where β^* is a factor describing how the water density is affected by the salt concentration. The parameter C_{max} denotes the maximum salt concentration, whereas a is a parameter controls the increase in density with salt concentration. The symbols β_{wp}, β_{wT}, p_{wo} and T_o represent the coefficient of water compressibility, the coefficient of volumetric thermal expansion, the reference pore water pressure and the reference temperature, respectively.

The evolution of the water density in time is derived as:

$$\frac{\partial \rho_w^l}{\partial t} = \frac{\partial \rho_w^l}{\partial T}\frac{\partial T}{\partial t} + \frac{\partial \rho_w^l}{\partial p_w}\frac{\partial p_w}{\partial h_w}\frac{\partial h_w}{\partial t} + \frac{\partial \rho_w^l}{\partial C}\frac{\partial C}{\partial t} = -\beta_{wT}\rho_w^l \frac{\partial T}{\partial t} + \beta_{wp} g \rho_w^l \rho_{wo}^l \frac{\partial h_w}{\partial t} + \rho_{wf}^l \frac{a}{C_{max}}\frac{\partial C}{\partial t}$$

5.

The pore water pressure is given as $p_w = g\rho_{wo}^l h_w$, where g is the gravity acceleration, h_w is the water pressure head and ρ_{wo}^l is the reference distilled water density at the atmospheric pressure and the reference temperature T_o = (273.16 + 20)K. The density of the distilled water at any temperature and water pressure is indicated by ρ_{wf}^l.

Moreover, the presence of salt in water affects, in particular, the gravitational component of the Darcian flux which is re-written as $\boldsymbol{q}^l = -K_l(\boldsymbol{\nabla} h_w + \beta^*)$ where K_l is the water hydraulic conductivity.

2. Mass balance equation of the dry air component:

$$n\rho_a[S^g + HS^l]\beta_{sT}\frac{\partial T}{\partial t} + \frac{\rho_a[S^g + HS^l]}{1-n}\frac{\partial n}{\partial t} + n[S^g + HS^l]\frac{\partial \rho_a}{\partial t} + n\rho_a[H-1]\frac{\partial S^l}{\partial t} + n\rho_a S^l\frac{\partial H}{\partial T}\frac{\partial T}{\partial t} + \boldsymbol{\nabla} \cdot (\rho_a \boldsymbol{q}^g) + \boldsymbol{\nabla} \cdot (\rho_a H \boldsymbol{q}^l) - \boldsymbol{\nabla} \cdot \boldsymbol{j}_w^g = 0 \quad (6)$$

where ρ_a and H denote the dry air density and Henry's volumetric coefficient of solubility, respectively.

The above equations require constitutive relationships (soil water retention curve, mechanical constitutive model, velocity and pressure head relationship etc.) to quantify $\frac{\partial S^l}{\partial t}$, $\frac{\partial \varepsilon_v}{\partial t}$, $\boldsymbol{q}^l$ and $\boldsymbol{q}^g$. The used constitutive equations are summarized in Table 1.

Table 1. Summary of the employed constitutive equations for fluid, thermal and salt transport.

Fluid flow

Darcy's law:

$\boldsymbol{q}^i = -K_i(\boldsymbol{\nabla} h_i + \beta^*)$

Water retention curve ((Van Genuchten, 1980)):

$S^l = (S^l_{sat} - S^l_{res})[1 + (g_\alpha|\psi|)^{g_n}]^{g_m} + S^l_{res}$

S^l_{sat}, S^l_{res}: degree of saturation at full and residual state

Relative permeability (Börgesson and Hernelind, 1999):

$K^l = K^l_{sat}\left(\frac{S^l - S^l_{res}}{S^l_{sat} - S^l_{res}}\right)^3$

$S^l + S^g = 1$

$g_\alpha = (\sigma^t_o/\sigma^t)g_{\alpha o}; \quad g_n = \frac{g_{no}}{1 - \xi^T_n g_{no}(T - T_o)}; \quad g_m = \frac{1}{g_n} - 1$

$S^l_{so} = S^l_{sat} + \xi^T_w(T - T_o); \ \sigma^t = 0.118 - 1.54 \times 10^{-4}\, T$

K_i and S^i: permeability and degree of saturation of fluid $i = l, g$

g_α, g_n, g_m, ξ^T_w, ξ^T_n and S^l_{so}: van Genuchten parameters with thermal effects (Jacinto *et al.*, 2009; Abed and Sołowski, 2017).

h_w, h_g and ψ: water pressure head, gas pressure head and suction head $\psi = h_g - h_w$.

σ^t: water surface tension.

Vapour diffusion

(Philip and De Vries, 1957):

$$\boldsymbol{j}^g_w = \underbrace{-D_{vw}\boldsymbol{\nabla} h_w + D_{vw}\boldsymbol{\nabla} h_g}_{moisture\ term} - \underbrace{D_{vT}\boldsymbol{\nabla} T}_{temperature\ term}$$

Note: D_{vw} and D_{vT} are diffusion coefficients that are dependent on soil tortuosity τ, thermal enhancement factor f_{Tv}, degree of saturation, soil porosity and molecular diffusivity of water vapour in air D_{atm}.

Heat flow

Fourier's law:

$\boldsymbol{q}^T = -\lambda_T \boldsymbol{\nabla} T$

$\lambda_T = \lambda^{S^l}_{sat}\lambda^{S^g}_{dry}$

λ_T, λ_{sat} and λ_{dry} : average, saturated and dry thermal conductivities.

Salt diffusion

Modified Fick's law:

$\boldsymbol{j}^l_{st} = -S^l n D_h \boldsymbol{\nabla} C$

D_h: dispersion coefficient, given as:

$D_h = \tau D_o + \alpha|\boldsymbol{v}^l|; \quad \boldsymbol{v}^l = \frac{\boldsymbol{q}^l}{nS^l}$

D_o: molecular diffusion coefficient.

α: dispersivity and $\boldsymbol{v}^l$: average liquid velocity.

3. Mass balance equation of salt component:

Upon examining Equation 1, it is clear that the general salt mass balance equation is the sum of contributions related to the crystallised (adsorbed) salt in the solid phase and the dissolved part in the liquid phase. For the salt in the solid phase, Equation 1 is written as:

$$\frac{\partial(\phi^s\rho^s\omega_{st}^s)}{\partial t} + \nabla\cdot(\phi^s\rho^s\omega_{st}^s\boldsymbol{v}^s) + \nabla\cdot\boldsymbol{j}_{st}^s = Q_{st}^s$$

7.

It is assumed in Equation 7 that the solid salt is not exposed to any chemical reactions that could affect the mass balance. Similarly, for the dissolved salt in the liquid phase, Equation 1 yields:

$$\frac{\partial(\phi^l\rho^l\omega_{st}^l)}{\partial t} + \nabla\cdot(\phi^l\rho^l\omega_{st}^l\boldsymbol{v}^l) + \nabla\cdot\boldsymbol{j}_{st}^l = Q_{st}^l$$

8.

Noticing that any adsorbed mass of salt should result in an equal loss in the dissolved salt mass and vice versa with $Q_{st}^s = -Q_{st}^w$ and assuming that the soil is deforming slowly with $\boldsymbol{v}^s \approx 0$, summing Equations 7 and 8 eventually gives the governing salt mass balance equation:

$$\frac{\partial\big((1-n)\rho^sC_s\big)}{\partial t} + \frac{\partial(nS^lC)}{\partial t} + [nS^lC + (1-n)\rho^sC_s]\frac{\partial\varepsilon_v}{\partial t} + \nabla\cdot(\boldsymbol{q}^lC) - \nabla\cdot(nS^lD_h\nabla C) = 0$$

9.

where ρ^s is the solid particles density. The mechanical coupling emerges through the volumetric deformation ε_v and porosity n. The dispersion coefficient D_h includes the molecular diffusion and the mechanical dispersion, where:

$$D_h = \tau D_o + \alpha|\boldsymbol{v}^l|; \quad \boldsymbol{v}^l = \frac{\boldsymbol{q}^l}{nS^l}$$

10.

The symbols τ, D_o, α and $\boldsymbol{v}^l$ denote tortuosity, the molecular diffusion coefficient, dispersivity and the average liquid velocity, respectively. Tortuosity is a measure of the geometric complexity of a porous geomaterial, which allows for the consideration of the effective path

length available for liquid flow. The adsorbed concentration (amount of salt per unit mass of solids) C_s (kg/kg) is assumed to correlate linearly with the dissolved concentration C (kg/l) through a distribution coefficient K_d (l/kg) where $C_s = K_d C$.

This study adopts the fully coupled formulation, which accounts for the spatial variation in water density. That is shown, for example, in Equation 2 upon expanding the term $\boldsymbol{\nabla} \cdot (\rho_w^l \boldsymbol{q}^l) = \rho_w^l (\boldsymbol{\nabla} \cdot \boldsymbol{q}^l) + \boldsymbol{q}^l \cdot (\boldsymbol{\nabla} \rho_w^l)$**.** Neglecting the spatial variation in water density (e.g. $\boldsymbol{\nabla} \rho_w^l = 0$) is known as Boussinesq approximation. Johannsen (2003) shows that such approximation leads to remarkable differences in the estimated flow field and consequently to a different salt concentration profile.

2.2 Energy balance equation

The enthalpy balance equation is given as follows (Thomas and He, 1997; Rutqvist *et al.*, 2001; Collin *et al.*, 2002; Abed and Sołowski, 2017):

$$\underbrace{\frac{\partial \Phi_h}{\partial t}}_{Heat\ storage} + \underbrace{L Q_w^g}_{latent\ heat\ of\ vaporization} + \underbrace{\boldsymbol{\nabla} \cdot \boldsymbol{q}_h}_{heat\ due\ to\ conduction\ and\ convection} = 0$$

11.

where Φ_h is the soil heat capacity and $\boldsymbol{q}_h$ is the heat flux including conduction and convection. Symbol L represents the latent heat of water vaporization and Q_w^g is the rate of water vapour production which can be derived based on Equation 1. The constitutive relationships related to the heat flow and the soil thermal conductivity are given in Table 1. The soil heat capacity is derived by adopting a suitable thermodynamic state function that requires the specific heat capacities of each soil components to be used (Diersch and Kolditz, 2002).

2.3 Mechanical Balance Equation

The local static mechanical balance equation is given as:

$$\boldsymbol{\nabla} \cdot \boldsymbol{\sigma}^{tot} + \boldsymbol{b} = 0$$

12.

where $\boldsymbol{\sigma}^{tot}$ and $\boldsymbol{b}$ stand for the total stresses and the body forces at a certain point of the domain, respectively. The body forces are usually due to the self-weight which is related to the density. To calculate the developed stresses as a result of the applied loading increment (chemical, thermal, hydraulic or mechanical load), a suitable constitutive model for unsaturated soil is needed. The current study employs an extended version of the Barcelona Basic Model (BBM) that accounts for thermal effects on mechanical behaviour (Alonso *et al.*, 1990; Gens, 1995; Laloui and Cekerevac, 2003). Appendix A gives an introduction to the BBM framework, though the interested reader may like to check the full description of the model and the numerical implementation given in previous publications (e.g. Abed, 2008; Sołowski and Gallipoli, 2010; Sołowski *et al.*, 2012; Sołowski and Sloan, 2013; Abed *et al.*, 2016; Abed and Sołowski, 2017).

2.4 Solution strategy

The finite element method is employed to discretise the balance Equations 2, 6, 9, 11 and 12 while a fully implicit finite differences scheme (backward Euler method) is used for the time discretisation. The resulting coupled system of nonlinear algebraic equations is solved using Newton-Raphson iterations.

This formulation is implemented into a computer code “Thebes Code” (Abed and Sołowski, 2017; Abed *et al.*, 2018) based on the NUMERRIN numerical solver (Laitinen, 2013). The code has logical switches that allow activating or deactivating any of the aforementioned balance equations to accommodate the nature of the treated problem.

3. Numerical applications with Thebes Code

The following sections illustrate results of two numerical applications that are generated using Thebes Code.

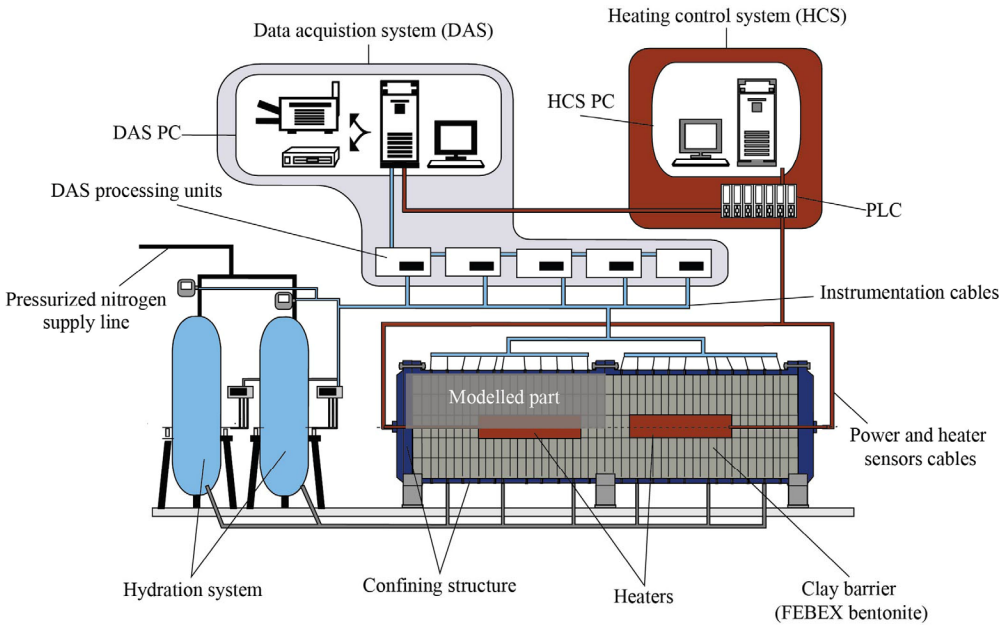

Figure 2. Details of CIEMAT mock-up test (modified after Martin *et al.* (2006)).

3.1 Application 1: Modelling of THM coupling (CIEMAT experiment)

Within the framework of FEBEX research project (Huertas *et al.*, 2000), CIEMAT (Madrid, Spain) performed a full scale mock-up test with controlled boundary conditions that resemble the real in-situ situation of nuclear waste barrier (Martin *et al.*, 2006). As shown in Figure 2, the test used two electrical heaters to simulate the temperature produced by the nuclear waste canisters. These were surrounded by a clay barrier made from the compacted “FEBEX” bentonite blocks. The test was fully instrumented with an automatic control of the heater temperature, sensors to measure the evolution of the main variables in the system (temperature, relative humidity, stresses etc.) and a data acquisition system to record and process the collected data by the sensors. Due to symmetry, only the indicated part in Figure 2 is numerically modelled in axisymmetric conditions.

The average initial water content of the bentonite blocks is 14%, which corresponds to the initial suction value of about 120MPa. Their initial dry density is 1770.0 Kg/m^3 and the total mass of bentonite used in the test is 22.5t. The dry density of bentonite decreases after saturation to an average targeted value of 1650 Kg/m^3 after the closure of the gaps between the blocks due to the bentonite swelling.

After an initial saturation phase, the heaters are put to work in three stages: (i) in the first 6 days they are subjected to an electrical power of 250W per heater, (ii) in the following 4 days the power is increased to 500W/heater, (iii) after this initial phase, the temperature is automatically controlled so that it stays at 100°C throughout the experiment operational life. A special system (see Figure 2) ensured continuous hydration of the bentonite through the outer boundaries by applying water under 0.55MPa pressure. Due to the limited data, the numerical simulation is only performed for the first 2500 days of the test duration.

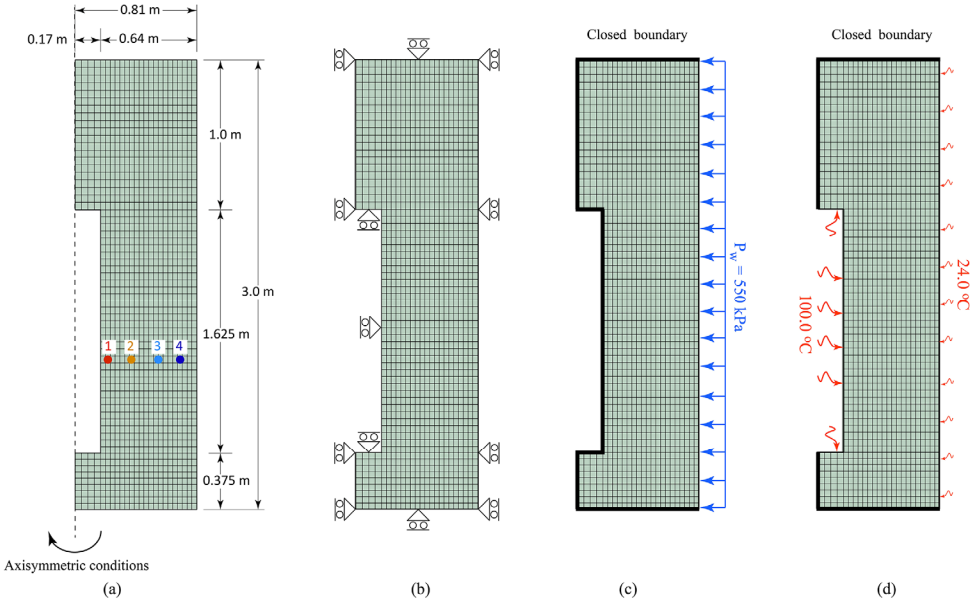

Figure 3. Finite element model of the mock-up test: (a) mesh and dimensions; (b) mechanical boundary conditions; (c) hydraulic boundary conditions; (d) thermal boundary conditions.

3.1.1 Finite element model

Figure 3 shows the finite element model used in the simulation. The sensitivity study of the solution with respect to the mesh density has shown that there was no significant change in the results when a denser mesh than the selected finite element mesh was used. Therefore, the analysis adopted a mesh made from 1396 4-noded quadrilateral elements with four integration points per element; see Figure 3(a). Thebes Code performs regular infinitesimal strain incremental analysis followed by updating the coordinates of the nodes. The updated mesh is used in the next loading step, which allows for capturing the influence of changing geometry on the results. Nonetheless, the deformations in the current problem are small and there is almost

no change in the results for analysis using classical small strain and the one with the mesh update.

To simulate constant volume conditions the model is constrained in the directions normal to its boundaries as depicted in Figure 3(b). The hydraulic and thermal boundary conditions are illustrated in Figure 3(c) and (d), respectively. The thermal load in the simulation has been applied to replicate the experiment. Therefore, the boundary near the heater is first subjected to total of 250W followed by 500W of energy flux during the first ten days. After that, the thermal boundary condition is changed to the prescribed temperature of 100^{o}C. The outer boundary of the model is kept at the prescribed temperature of 24^{o}C which simulates the recorded average room temperature. As no gas pressure measurements are provided, the gas pressure is assumed to stay atmospheric everywhere in the solved domain. An initial stress of 10kPa is assigned to the bentonite that simulates the average bentonite self-weight in the middle of the container. Only Equations 2, 11 and 12 are active in this analysis yielding a coupled thermo-hydro-mechanical problem.

Table 2. FEBEX bentonite properties as used in the analysis (for a better understanding of the mechanical parameters see Appendix A)

(a) Mechanical properties

ν	κ_o	κ_{so}	n	$\alpha_o[1/\mathrm{K}]$	γ_T	α_2	α_k	α_{ks1}	α_{ks2}
0.4	0.05	0.3	0.35	1.5E-4	0.25	0.0	-3.0E-6	-0.147	0.0

M	k	p^c_{ref}[kPa]	λ	$\beta[1/\mathrm{kPa}]$	r	p^c[kPa]	ρ^T	p^*_o[kPa]
1.0	0.1	12.0	0.15	1.0E-4	0.925	500.0	0.2	1.2E+4

(b) Hydraulic properties

$g_{ao}[1/\mathrm{m}]$	g_{no}	S^l_{res}	S^l_{sat}	$\xi^T_n[1/\mathrm{K}]$	$\xi^T_w[1/\mathrm{K}]$	K^l_{sat}[m/s]
3.5E-04	1.22	0.0	1.0	-1.0E-4	-1.5E-3	1.9E-14

(c) Thermal properties

λ_{sat}[W/m/K]	λ_{dry}[W/m/K]	τ	f_{Tv}
1.15	0.47	0.87	1.0

3.1.2 FEBEX bentonite properties

The FEBEX bentonite has been thoroughly tested to establish its relevant thermal, hydraulic, mechanical and chemical properties, including Gens *et al.* (2009), Villar and Gómez-Espina (2009), Sánchez and Gens (2014). Data from these publications are used to calibrate the required model parameters, which are listed in Table 2. The derived parameters are in the ranges of the typical values for FEBEX bentonite (CODE-BRIGHT, 2002; Toprak *et al.*, 2012; Sánchez and Gens, 2014). The extra parameters ξ_n^T and ξ_w^T that account for the effect of temperature on the water retention curve (see Table 1) are calibrated based on data by Jacinto *et al.* (2009) and the measurements of CIEMAT test.

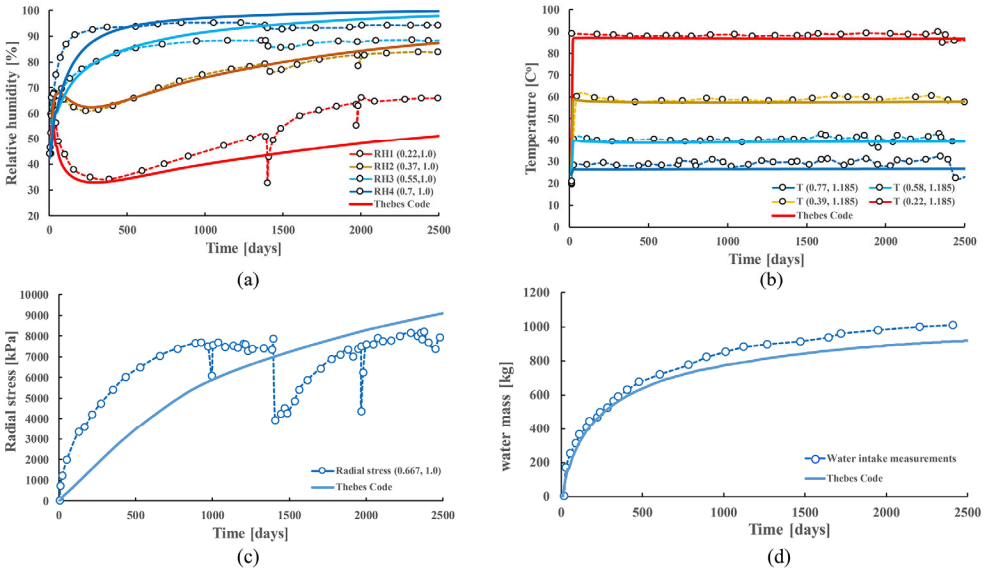

Figure 4. Numerical results versus measurements: (a) relative humidity; (b) temperature; (c) swelling pressure; (d) water intake.

3.1.3 Discussion of numerical predictions

The numerical results at the control points 1, 2, 3 and 4 in Figure 3(a) are depicted in Figure 4. These numerical results are compared to the experimental measurements given by Martin *et al.*

(2006). In Figure 4(a) the code predictions are in a good agreement with the relative humidity measurements, especially during the first 500 days. After that, the numerical predictions deviate from measurements showing faster hydration. The temperature obtained in the simulation is in very good agreement with the temperature measurements as can be seen in Figure 4(b). Similarly, the water intake is predicted very well, as shown in Figure 4(d). However, the swelling pressure predictions in Figure 4(c) are less satisfactory. Even though the swelling pressure value at 2500 days is recovered fairly well, the code gives too low values of the swelling pressure during the initial stages of the test. That can be partially related to microstructure effects upon hydration, which are not taken into account in the mechanical model in the simulation. Figure 5 shows porosity, degree of saturation and temperature distribution at 2500 days of experiment life.

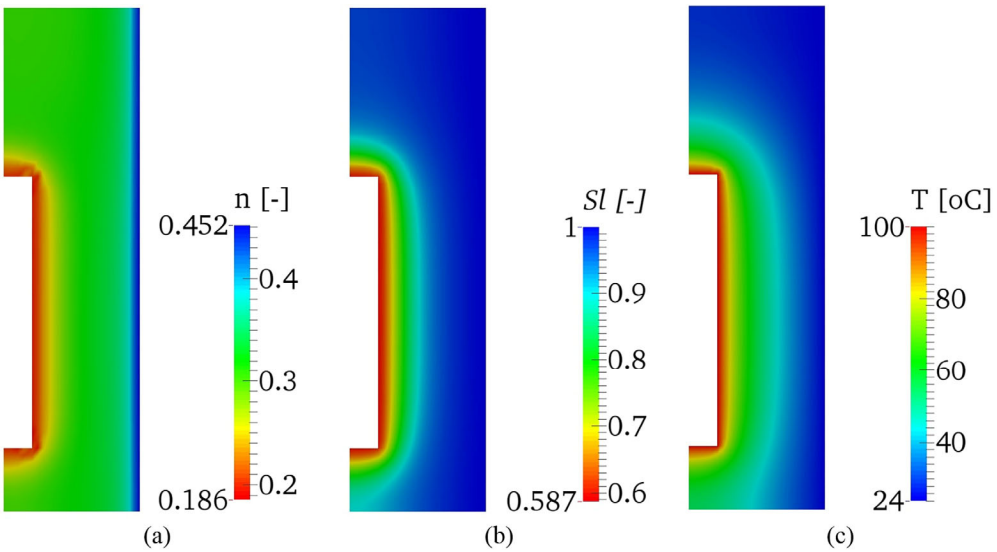

Figure 5. Basic variables distribution after 2500 days of experiment inception: (a) porosity (n); (b) degree of saturation S^l; (c) temperature (T).

3.2 Application 2: Modelling of Hydro-Chemical coupling (Elder problem)

The Elder problem (Elder, 1967) is a convection problem originally designed to study the laminar fluid flow initiated by thermally induced water density gradient. The problem was later adjusted by Voss and Souza (1987) for the simulation of a density-driven salt transport. Since that time, it became a typical benchmark to verify the performance of the computer codes (Boufadel *et al.*, 1999; Diersch and Kolditz, 2002; Van Reeuwijk *et al.*, 2009). The Elder problem

is challenging due to bifurcation and its sensitivity to the imposed boundary conditions, used mesh and time step. A comprehensive overview on the matter can be found in Park and Aral (2007) and Van Reeuwijk *et al.* (2009).

Despite the possible bifurcation, certain finite element mesh configurations and time stepping scheme (Johannsen, 2003) provided stable steady state solutions which are adopted in this study as a reference. Furthermore, the comparison also uses results for the transient phase by Voss and Souza (1987) and Guo and Langevin (2002).

3.2.1 Finite element model

Figure 6 shows the geometry, boundary conditions and the finite element mesh employed in this analysis. The problem is plane strain and, due to symmetry, only half of the problem is analysed. The physical properties in the analysis are listed in Table 3. The simulation assumes the soil to be fully saturated with $S^l = 1.0$ during the analysis. The problem is also isothermal and the soil matrix is considered non-deformable. Therefore, only Equation 2 and Equation 9 are active and solved together yielding a coupled hydro-chemical problem. The boundaries are closed with respect to water flow, with imposed zero water pressure head ($h_w = 0$) enforced along a small 0.2m part of the upper boundary, see Figure 6. That represents point-like condition when compared to the other problem dimensions. The bottom boundary has a prescribed zero salt concentration while the central 300.0 meters of the upper boundary are subjected to a maximum salt concentration of $C_{max} = 310.0$g/l. The analysis investigates the system behaviour over a total period of 100 years. To show the effect of the mesh and the time stepping on the numerical results, the analysis is performed twice. In the first run which will be referred to as *coarse discretisation* case, the mesh is relatively coarse and consisting of 40x100 (4000) four-noded quadrilateral finite elements with four Gauss integration points per element. The simulation time step increases in time: the time step of Δt = 15 days is employed during the first two years, the time step Δt = 60 days in the range 2 years $< t \leq$ 20 years and, finally, the time step Δt = 576 days in the range 20 years $< t \leq$ 100 years. This time stepping arrangement yields a total number of 206 time steps. In the second run which will be referred to as *fine discretisation* case, finer mesh and time steps are used with 200x800 (160000) elements and fixed time step of Δt = 15 days throughout the analysis (total number of 2400 time steps).

According to Johannsen (2003) the *coarse discretisation* should lead to a steady state with salt concentration showing one finger in the middle of the solution domain being known as S1 configuration, while the *fine discretisation* should lead to S2 configuration with two fingers of the salt concentration.

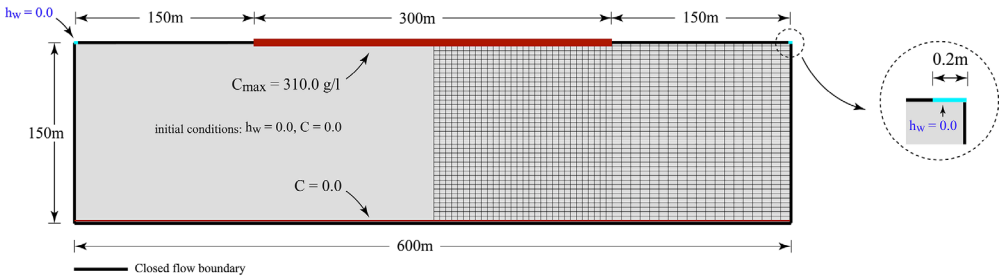

Figure 6. Finite element model for Elder problem.

Table 3. Physical properties for Elder problem.

n	$K_l[m/s]$	$D_o[m^2/s]$	α	K_d	τ	a	$\rho_{wo}^{l}[kg/m^3]$	$\mu_l[\frac{kg}{m}/s]$	$g[m/s^2]$
0.1	4.7026E-6	3.565E-6	0.0	0.0	1.0	0.2	998.2	0.001009	9.81

3.2.2 Discussion of the numerical results

Considering the hydraulic boundary conditions alone and neglecting the coupling effects, no water flow is expected to occur. Moreover, the salt is expected to gradually diffuse from the high to low concentration boundaries. This situation is achieved in this example by putting a = 0 in Equation 4 which removes any effect of salt concentration on the water density. Figure 7 shows the perfect match between the calculated steady state in this case and the reference solution by Johannsen (2003). It is worthwhile to mention that the solution here is the same for both coarse and fine discretisation cases.

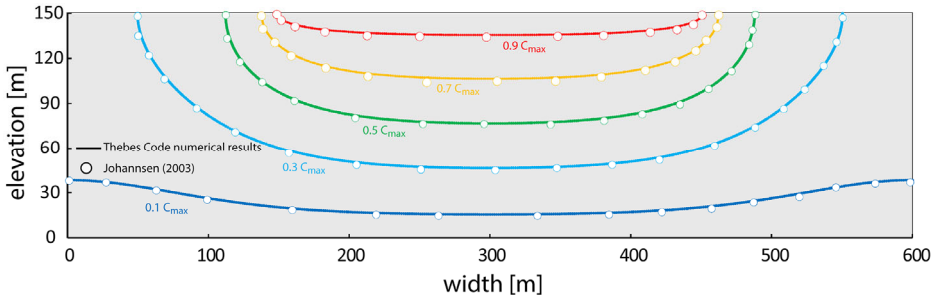

Figure 7. Calculated salt concentration at steady state versus reference results by Johannsen (2003) in case of decoupled hydro-chemical calculations (a = 0).

The situation clearly changes upon considering coupling and putting α = 0.2. By doing so, the water density ultimately reaches 1.2 times its initial value. The gradual increase in water density due to the increase of salt concentration triggers water flow due to the spatial variation of β^* value in the domain. The new water flow pattern, in turn, affects the salt diffusion process and so on and so forth. Figure 8 shows a perfect match in this case at the steady state case compared to the reference results for the *coarse discretisation* case where S1 configuration is recovered.

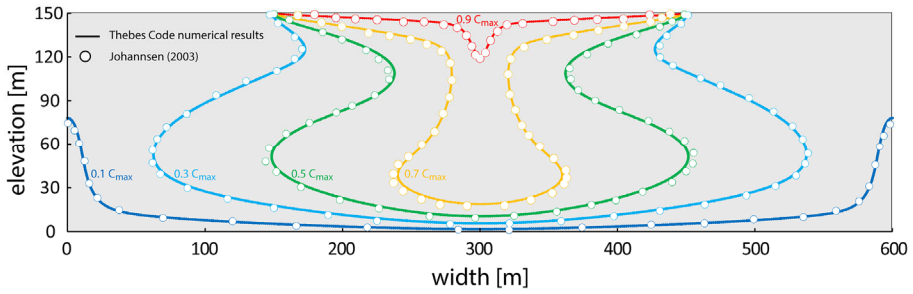

Figure 8. Calculated salt concentration at steady state versus reference results by Johannsen (2003) in case of coupled hydro-chemical calculations (α = 0.2) and *coarse discretisation*.

Additionally, Figure 9 shows that the Thebes Code results match well other published results (Voss and Souza,1987; Guo and Langevin, 2002) with comparable coarse discretisation during the transient phase (at t = 10 years). The differences are partially explained by the different meshes, time stepping and finite element types employed by the authors. However, bearing in mind the sensitivity of the Elder problem to such variations, the solutions match well. The calculated salt concentration distribution at different time steps is given in Figure 10. The graphical output in Figure 10 is produced with the freely available ParaView visualization software (Henderson *et al.*, 2004).

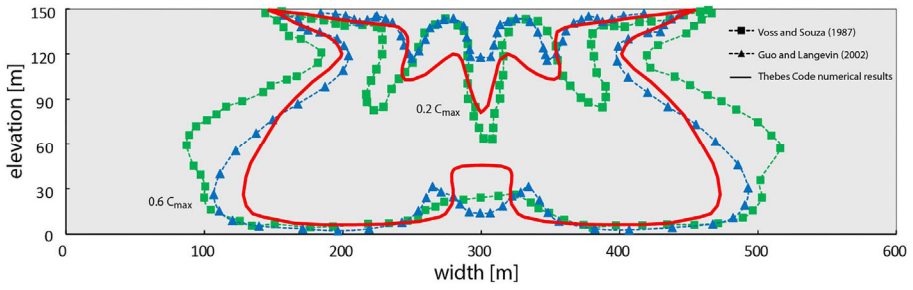

Figure 9. Calculated salt concentration after 10 years compared to published data.

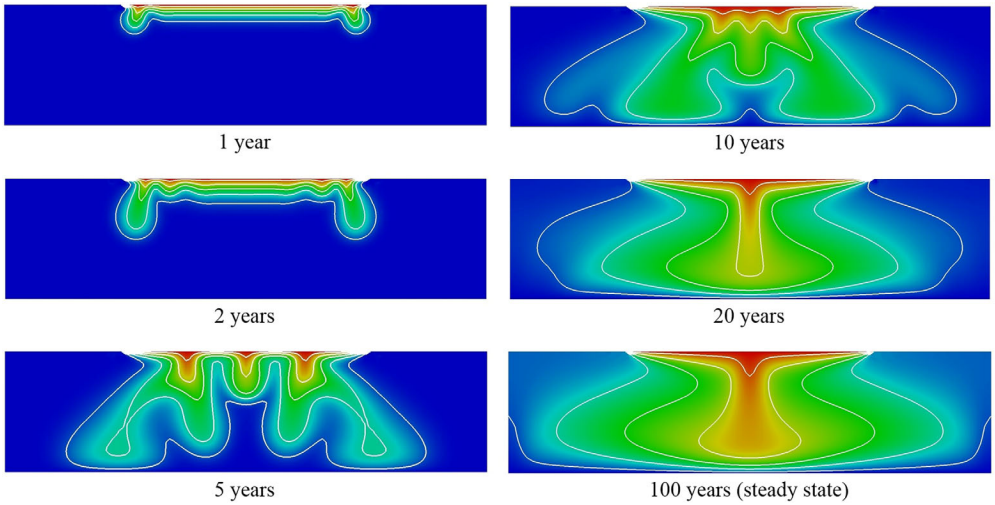

Figure 10. Calculated salt concentration at different time steps in case of *coarse discretisation* (contour lines represent from top to bottom: 0.9C_{max}, 0.7C_{max}, 0.5C_{max}, 0.3C_{max} and 0.1C_{max} where C_{max} = 310.0g/l).

The Thebes Code results also match perfectly the steady state that involves S2 configuration in the case of *fine discretisation* as it is clear in Figure 11. The evolution of salt concentration profile over time is shown in Figure 12 in this case.

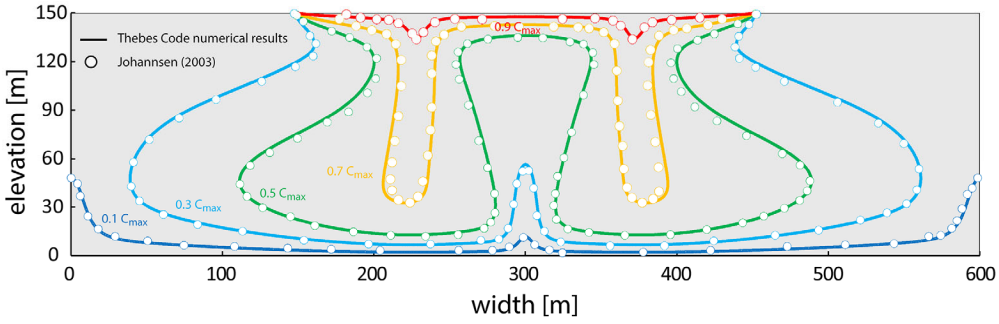

Figure 11. Calculated salt concentration at steady state versus reference results by Johannsen (2003) in case of coupled hydro-chemical calculations (α = 0.2) and *fine discretisation*.

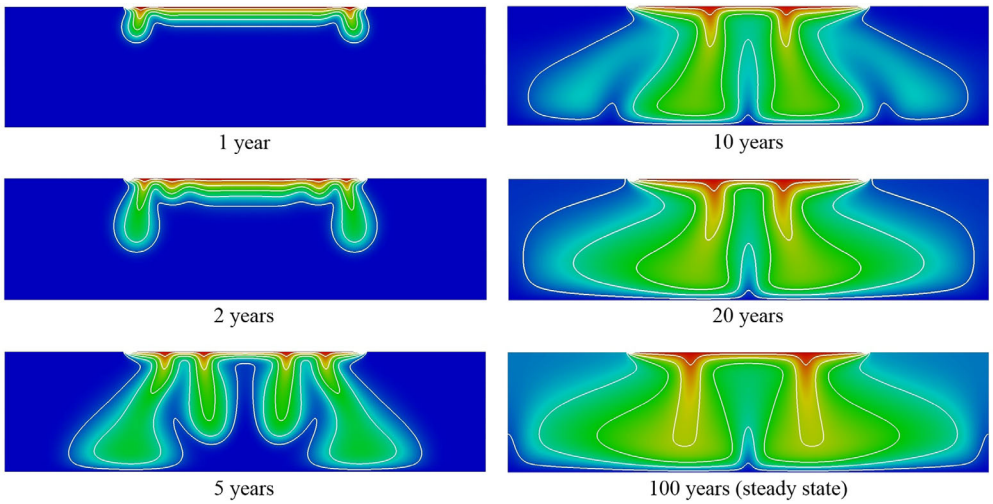

Figure 12. Calculated salt concentration at different time steps in case of *fine discretisation* (contour lines represent from top to bottom: $0.9C_{max}$, $0.7C_{max}$, $0.5C_{max}$, $0.3C_{max}$ and $0.1C_{max}$ where C_{max} = 310.0g/l).

4. Conclusions

This article illustrates the performance of a newly developed fully coupled THMC code through the simulation of the well-known Elder problem and the well-documented CIEMAT mock-up test. The numerical results show that Thebes Code is capable of providing reliable predictions for the bentonite behaviour in complex environmental conditions, as in the case of nuclear waste barriers. However, the adopted framework still needs improvement to consider properly the role and evolution of bentonite microstructure. That is the aim of the ongoing research (Abed and Sołowski, 2018), which will improve the constitutive relationships for mechanical behaviour of bentonite, water, heat and salt transport.

Acknowledgements

The authors would like to gratefully acknowledge that the presented research has been funded by KYT2018 Finnish Research Programme on Nuclear Waste Management via THEBES project.

References

Abed A (2008) *Numerical modeling of expansive soil behavior* (PhD thesis). Institut für Geotechnik (IGS), Universität Stuttgart, Germany.

Abed A and Sołowski W (2017) A study on how to couple thermo-hydro-mechanical behaviour of unsaturated soils: Physical equations, numerical implementation and examples. *Computers and Geotechnics* **92**: 132–155.

Abed A and Sołowski W (2018) Material Microstructure Effects in Thermo-Hydro-Mechanical Modelling of Bentonite. In *PanAm Unsaturated Soils 2017 (Fundamentals)*. GSP 301. ASCE, pp. 330–339.

Abed A, Laitinen M, Lämsä J, Harjupatana T, Sołowski W and Kataja M (2016) Hydro-mechanical modelling of MX-80 bentonite: one dimensional study. *Proceedings of E-UNSAT 2016*, *Paris, France*.

Abed A, Sołowski W, Gens A and Romero E (2018) Inclusion of chemical effect in a fully coupled THM finite element code. *Proceedings of UNSAT2018*, Hong Kong.

Ahmad P (2017) Environmental geotechnics in modern societies. *Environmental Geotechnics* **4(6)**: 393–394.

Alonso E, Gens A and Josa A (1990) A constitutive model for partially saturated soils. *Géotechnique* **40(3)**: 405–430.

Börgesson L and Hernelind J (1999) *Äspö Hard Rock Laboratory: International Progress Report*. Preliminary modelling of the water saturation phase of the buffer and backfill materials. Swedish Nuclear Fuel and Waste Management Company, Stockholm, Sweden, IPR-00-11.

Boufadel M, Suidan M and Venosa A (1997) Density-dependent flow in one-dimensional variably-saturated media. *Journal of hydrology* **202(1)**: 280–301.

Boufadel M, Suidan M and Venosa A (1999) Numerical modeling of water flow below dry salt lakes: effect of capillarity and viscosity. *Journal of Hydrology* **221(1–2)**: 55–74.

CODE-BRIGHT (2002) *3D program for thermo-hydro-mechanical analysis in geological media, user's guide*. Universitat Politècnica de Catalunya (UPC), Barcelona, Spain.

Collin F, Li X, Radu J and Charlier R (2002) Thermo-hydro-mechanical coupling in clay barriers. *Engineering Geology* **64(2)**: 179–193.

Darcy H (1856) *Les Fontaines Publiques de La Ville de Dijon, Dalmont*. Paris: Dalmont.

Diersch H and Kolditz O (2002) Variable-density flow and transport in porous media: approaches and challenges. *Advances in water resources* **25(8)**: 899–944.

Elder J (1967) Transient convection in a porous medium. *Journal of Fluid Mechanics* **27(3)**: 609–623.

Esch J (2010) *Adaptive Multiscale Finite Element Method for Subsurface Flow Simulation* (PhD thesis). Delft University of Technology, Delft, Netherlands.

Gens A (1995) Constitutive Laws. In: *Modern issues in non-saturated soils*, Springer, Vienna, pp. 129–158.

Gens A, Sánchez M, Guimaraes L, Alonso E, Lloret A, Olivella S, Villar M and Huertas F (2009) A full-scale in situ heating test for high-level nuclear waste disposal: observations, analysis and interpretation. *Géotechnique* **59(4)**: 377–377.

Guo W and Langevin C (2002) *User's guide to SEAWAT; a computer program for simulation of three-dimensional variable-density ground-water flow*.

Henderson A, Ahrens J and Law C (2004) *The ParaView Guide*. Kitware Clifton Park, NY.

Huertas F, Fuentes-Cantillana J, Jullien F, Rivas P, Linares J, Fariña P, Ghoreychi M, Jockwer N, Kickmaier W, Martínez M and Samper J (2000) *Full-scale engineered barriers experiment for a deep geological repository for high-level radioactive waste in crystalline host rock* (FEBEX project), European Commission, Luxembourg City, Luxembourg, EUR.

Huyakorn P (2012) *Computational Methods in Subsurface Flow*. Academic Press.

Jacinto A, Villar M, Gómez-Espina R and Ledesma A (2009) Adaptation of the van Genuchten expression to the effects of temperature and density for compacted bentonites. *Applied Clay Science* **42(3)**: 575–582.

Jacinto A and Ledesma A (2017) Thermo-hydro-mechanical analysis of a full-scale heating test. *Environmental Geotechnics* **4(2)**: 123–134.

Johannsen K (2003) On the validity of the Boussinesq approximation for the Elder problem. *Computational Geosciences* **7(3)**: 169–182.

Laitinen M (2013) *Numerrin 4.0 Manual*. Numerola Oy, Jyväskylä, Finland.

Laloui L and Cekerevac C (2003) Thermo-plasticity of clays: an isotropic yield mechanism. *Computers and Geotechnics* **30(8)**: 649–660.

Laloui L, Klubertanz G and Vulliet L (2003) Solid-liquid-air coupling in multiphase porous media. *International Journal for Numerical and Analytical Methods in Geomechanics* **27(3)**: 183–206.

Martin P, Barcala J and Huertas F (2006) Large-scale and long-term coupled thermo-hydro-mechanic experiments with bentonite: the FEBEX mock-up test. *Journal of Iberian geology* **32(2)**: 259–282.

Olivella S, Carrera J, Gens A and Alonso E (1994) Nonisothermal multiphase flow of brine and gas through saline media. *Transport in porous media* **15(3)**: 271–293.

Olivella S, Gens A, Carrera J and Alonso E (1996) Numerical formulation for a simulator (CODE_BRIGHT) for the coupled analysis of saline media. *Engineering computations* **13(7)**: 87–112.

Panday S and Corapcioglu M (1989) Reservoir transport equations by compositional approach. *Transport in porous media* **4(4)**: 369–393.

Park C and Aral M (2007) Sensitivity of the solution of the Elder problem to density, velocity and numerical perturbations. *Journal of contaminant hydrology* **92(1–2)**: 33–49.

Philip J and De Vries D (1957) Moisture movement in porous materials under temperature gradients. *Eos, Transactions American Geophysical Union* **38(2)**: 222–232.

Rodriguez-Dono A, Olivella S and Mokni N (2018) Assessment of a high-level spent nuclear fuel disposal model. *Environmental Geotechnics*, https://doi.org/10.1680/jenge.18.00017.

Rutqvist J, Börgesson L, Chijimatsu M, Kobayashi A, Jing L, Nguyen T, Noorishad J and Tsang C (2001) Thermohydromechanics of partially saturated geological media: governing equations and formulation of four finite element models. *International journal of rock mechanics and mining sciences* **38(1)**: 105–127.

Sánchez M and Gens A (2014) *Modelling and interpretation of the FEBEX mock up test and of the long-term THM tests*. EU project: Long-term Performance of Engineered Barrier Systems PEBS: Deliverable D3.3-3, European Commission.

Sánchez M, Falcão F, Mack M, Pereira J, Narsilio G and Guimarães L (2017) Salient comments from an expert panel on energy geotechnics. *Environmental Geotechnics* **4(2)**: 135–142.

Seetharam S, Thomas H and Cleall P (2007) Coupled thermo/hydro/chemical/mechanical model for unsaturated soils-Numerical algorithm. *International Journal for Numerical Methods in Engineering* **70(12)**: 1480–1511.

Simpson M and Clement T (2003) Theoretical analysis of the worthiness of Henry and Elder problems as benchmarks of density-dependent groundwater flow models. *Advances in Water Resources* **26(1)**: 17–31.

Sołowski W and Gallipoli D (2010) Explicit stress integration with error control for the Barcelona Basic Model: Part I: Algorithms formulations. *Computers and Geotechnics* **37(1)**: 59–67.

Sołowski W and Sloan S (2013) Equivalent stress approach in creation of elastoplastic constitutive models for unsaturated soils. *International Journal of Geomechanics* **15(2)**: 04014041.

Sołowski W, Hofmann M, Hofstetter G, Sheng D and Sloan S. (2012) A comparative study of stress integration methods for the Barcelona Basic Model. *Computers and Geotechnics* **44**: 22–33.

Thomas H and He Y (1997) A coupled heat-moisture transfer theory for deformable unsaturated soil and its algorithmic implementation. *International Journal for Numerical Methods in Engineering* **40(18)**: 3421–3441.

Toprak E, Olivella S, Mokni M and Pintado X (2012) *Thermo-hydro-mechanical modelling of buffer.* Synthesis Report. Eurajoki, Finland. Posiva Report.

Toprak E, Olivella S and Pintado X (2018) Modelling engineered barriers for spent nuclear fuel repository using a double-structure model for pellets. *Environmental Geotechnics*, https://doi.org/10.1680/jenge.17.00086

Van Genuchten M (1980) A closed-form equation for predicting the hydraulic conductivity of unsaturated soils 1. *Soil science society of America journal* **44(5)**: 892–898.

Van Genuchten M (1982) A comparison of numerical solutions of the one-dimensional unsaturated—saturated flow and mass transport equations. *Advances in Water Resources* **5(1)**: 47–55.

Van Reeuwijk M, Mathias S, Simmons C and Ward J (2009) Insights from a pseudospectral approach to the Elder problem. *Water Resources Research* **45(4)**.

Villar M, Iglesias R and García-Siñeriz M (2018) State of the in situ Febex test (GTS, Switzerland) after 18 years: a heterogeneous bentonite barrier. *Environmental Geotechnics*, https://doi.org/10.1680/jenge.17.00093.

Villar M and Gómez-Espina R (2009) *Report on thermo-hydro-mechanical laboratory tests performed by CIEMAT on FEBEX bentonite 2004-2008*. Centro de Investigaciones Energeticas Medioambientales y Tecnologicas (CIEMAT), Madrid, Spain.

Voss C and Souza W (1987) Variable density flow and solute transport simulation of regional aquifers containing a narrow freshwater-saltwater transition zone. *Water Resources Research* **23(10)**: 1851–1866.

Warrick A, Biggar J and Nielsen D (1971) Simultaneous solute and water transfer for an unsaturated soil. *Water Resources Research* **7(5)**: 1216–1225.

Appendix A

This appendix gives a summary on the enhanced Barcelona Basic model (Alonso *et al.*, 1990; Gens, 1995; Laloui and Cekerevac, 2003) used in the analysis.

The net stress rate is determined as:

$$\dot{\boldsymbol{\sigma}} = \boldsymbol{D}^{\mathrm{e}}\dot{\boldsymbol{\varepsilon}} - \boldsymbol{D}^{\mathrm{e}}\boldsymbol{m}^{T}\frac{\kappa_s}{3v(s+P_{atm})}\dot{s} + \boldsymbol{D}^{\mathrm{e}}\boldsymbol{m}^{T}\frac{(\alpha_o+\alpha_2\Delta T)}{3}\dot{T} - \boldsymbol{D}^{\mathrm{e}}\dot{\Lambda}\frac{\partial Q}{\partial \boldsymbol{\sigma}}$$

where $\boldsymbol{D}^{\mathrm{e}}$ is the elasticity matrix which is dependent on the soil swelling index κ , isotropic net pressure $p = tr(\boldsymbol{\sigma})/3$, the specific volume v and Poisson's ratio ν. The symbols $\dot{\boldsymbol{\varepsilon}}$, $\boldsymbol{m}$, s, P_{atm} and $\dot{\Lambda}$ stand for total strain rate, unity vector, suction, atmospheric pressure and a plastic multiplier, respectively. The parameters κ_s , α_o and α_2 are the suction swelling index and thermal elastic expansion parameters, respectively. The temperature increment is denoted by ΔT.

In order to account for the swelling nature of some soils, the elastic stiffness is made pressure and suction dependent as follows:

$$\kappa = \kappa_o(1 + \alpha_\kappa s)$$

$$\kappa_s = \kappa_{so}\left(1 + \alpha_{\kappa s1}\ln\left(\frac{p}{p_{ref}^c}\right)\right)e^{\alpha_{\kappa s2}s}$$

where κ_o and κ_{so} are reference values of κ and κ_s, respectively. Extra material parameters α_κ , $\alpha_{\kappa s1}$, $\alpha_{\kappa s2}$ and p_{ref}^c are needed in this case.

The yield surface F is described by:

$$F = q^2 - M^2(p + p_s)(p_o - p) = 0$$

where M is the slope of critical state line and q stands for the deviatoric stress:

$$q = \frac{1}{\sqrt{2}}\sqrt{(\sigma_1 - \sigma_2)^2 + (\sigma_2 - \sigma_3)^2 + (\sigma_3 - \sigma_1)^2}\,,$$

where σ_1, σ_2 and σ_3 are the principal stresses. The plastic strain direction is determined by a plastic potential function Q:

$$Q = \alpha^* q^2 - M^2(p + p_s)(p_o - p) = 0$$

The factor α^* , which allows for the recovery of the Jaky's approximation of coefficient of at rest soil pressure K_0 in 1D compression, is defined as

$$\alpha^* = \frac{M(M-9)(M-3)}{9(6-M)}\frac{\lambda}{\lambda-\kappa},$$

where λ is the slope of normal consolidation line.

Extended thermal BBM assumes that the soil shear strength is affected by suction and temperature as follows:

$$p_s = kse^{-\rho^T \Delta T},$$

where ρ^T and k are material constants. The soil preconsolidation pressure p_o is also considered to be suction and temperature dependent through the equation:

$$p_o = p^c \left(\frac{p_{oT}^*}{p^c}\right)^{\frac{\lambda-\kappa}{\lambda_s-\kappa}}$$

with

$$\lambda_s = \lambda\left[(1-r)e^{-\beta s} + r\right]$$

and

$$p_{oT}^* = p_o^* \left(1 - \gamma_T \log\left(\frac{T}{T_o}\right)\right)$$

where the preconsolidation pressure at full saturation and at the reference temperature $T_o = 20\ ^oC$ is indicated by p_o^*. The parameters p^c, β, r, γ_T are material constants that have to be determined experimentally. Finally, the preconsolidation pressure is updated as:

$$p_o^* = p_{oi}^* e^{\frac{v\dot{\varepsilon}_p^v}{\lambda-\kappa}},$$

where p_{oi}^* is the initial preconsolidation pressure and $\dot{\varepsilon}_p^v = tr(\dot{\varepsilon}_p)$ is the plastic volumetric strain rate.